




Article

Utilising Artificial Neural Networks for Assessing Seismic Demands of Buckling Restrained Braces Due to Pulse-like Motions

Amirhossein Mohammadi ¹, Shaghayegh Karimzadeh ^{1,*}, Saman Yaghmaei-Sabegh ², Maryam Ranjbari ² and Paulo B. Lourenço ¹

¹ Department of Civil Engineering, ARISE, Institute for Sustainability and Innovation in Structural Engineering (ISISE), University of Minho, 4800-058 Guimarães, Portugal; id9251@alunos.uminho.pt (A.M.); pbl@civil.uminho.pt (P.B.L.)

² Department of Civil Engineering, University of Tabriz, Tabriz 5166616471, Iran; s_yaghmaei@tabrizu.ac.ir (S.Y.-S.); maryamranjbari@yahoo.com (M.R.)

* Correspondence: shaghkn@civil.uminho.pt

Abstract: Buckling restrained brace frames (BRBFs) exhibit exceptional lateral stiffness, load-bearing capacity, and energy dissipation properties, rendering them a highly promising choice for regions susceptible to seismic activity. The precise and expeditious prediction of seismic demands on BRBFs is a crucial and challenging task. In this paper, the potential of artificial neural networks (ANNs) to predict the seismic demands of BRBFs is explored. The study presents the characteristics and modelling of prototype BRBFs with different numbers of stories and material properties, utilising the OpenSees software (Version 2.5.0) for numerical simulations. The seismic performance of the BRBFs is evaluated using 91 near-fault pulse-like ground motions, and the maximum inter-storey drift ratio (*MIDR*) and global drift ratio (*GDR*) are recorded as a measure of seismic demand. ANNs are then trained to predict the *MIDR* and *GDR* of the selected prototypes. The model's performance is assessed by analysing the residuals and error metrics and then comparing the trend of the results with the real dataset. Feature selection is utilised to decrease the complexity of the problem, with spectral acceleration at the fundamental period (T) of the structure (S_a), peak ground acceleration (*PGA*), peak ground velocity (*PGV*), and T being the primary factors impacting seismic demand estimation. The findings demonstrate the effectiveness of the proposed ANN approach in accurately predicting the seismic demands of BRBFs.

Keywords: pulse-wise real ground motion records; buckling restrained brace frame (BRBF); maximum inter-storey drift ratio (*MIDR*); global drift ratio (*GDR*); feature selection; artificial neural network (ANN)



Citation: Mohammadi, A.; Karimzadeh, S.; Yaghmaei-Sabegh, S.; Ranjbari, M.; Lourenço, P.B. Utilising Artificial Neural Networks for Assessing Seismic Demands of Buckling Restrained Braces Due to Pulse-like Motions. *Buildings* **2023**, *13*, 2542. <https://doi.org/10.3390/buildings13102542>

Academic Editor: Giuseppina Uva

Received: 4 September 2023

Revised: 3 October 2023

Accepted: 6 October 2023

Published: 8 October 2023



Copyright: © 2023 by the authors. Licensee MDPI, Basel, Switzerland. This article is an open access article distributed under the terms and conditions of the Creative Commons Attribution (CC BY) license (<https://creativecommons.org/licenses/by/4.0/>).

1. Introduction

Throughout history, the built environment has experienced significant human casualties and economic losses due to the destructive nature of earthquakes. Researchers have focused on developing innovative strategies to enhance building structural performance while also employing alternative approaches to estimate demands on structures and assess losses in the building stock [1–8]. In recent years, the rapid advancement of computer processors has led to a significant increase in the utilisation of machine learning capabilities across various engineering domains [9–19]. An important application of machine learning is to enable accurate and reliable estimation of seismic demands for single-degree-of-freedom or more complex multi-degree-of-freedom structures, an area of growing interest in recent times [20–24]. This capability holds great promise for reducing the time required for analyses and predictions, thereby enhancing overall efficiency. The literature review reveals that research efforts to predict structural responses have predominantly focused on conventional systems, such as moment-resisting frames. However, with

the emergence of new structural systems in recent years, there is a pressing need to explore their seismic demand.

Due to their better lateral stiffness during earthquakes and higher load capacity, bracing frames have received more attention from earthquake engineers than other structural frames [25]. Nevertheless, the buckling behaviour of the braces during compression causes a sharp reduction in their energy dissipation and load-bearing capacity. To deal with this disadvantage, the idea of a buckling restrained brace (BRB) was first proposed in Japan in the 1970s [26,27]. BRB has been widely used in the literature on bridge structures [28–32]. A BRB mainly consists of two parts: the core and restraining segments. Standing out over the entire axial force and dissipating energy is supplied by the core, while restraining segments prevent buckling of members in compression. Also, an unbounded material is employed between the core and restraining segments to be sure that the axial force is only resisted by the core. The core material plays an important role in the performance of BRBs under earthquake excitations. To provide the hysteresis behaviour of BRB, the core material should have sufficient ductility, strength, and stiffness while maintaining a lightweight profile. Carbon steel, low-yield-point steel, and aluminium alloys are the most used core materials. Restraining segments have different types, including reinforced concrete, concrete-filled steel tube, fibre-reinforced polymer, and all-steel assembled [33]. Stable lateral stiffness, sufficient energy dissipation, and comfortable replacement processes can be counted as the principal advantages of BRBs. Acting as a structural fuse under the maximum considered earthquake and improving the load capacity under the design basis of an earthquake can protect the structure [34].

This paper introduces a novel approach that employs machine learning techniques to estimate the seismic demands of buckling restrained brace frames (BRBFs). In contrast to the existing literature, the novelty lies in the utilisation of ANN for BRBFs. Therefore, this study represents a novel endeavour to predict seismic demand for BRBFs using machine learning techniques. By effectively training the ANN model, we aim to achieve precise predictions of the response behaviour of these specific structural systems, thereby addressing a critical research gap. The studied models of BRBs consist of a core for energy absorption and dissipation, along with restraining segments to prevent buckling. Various core materials, including carbon steel, low-yield-point steel, and aluminium alloys, are considered alongside different types of restraining segments like reinforced concrete and steel tubes. The paper presents the characterisation and modelling of these prototypes with varying numbers of stories and material properties, utilising the OpenSees software [35] for numerical simulations. Nonlinear force-beam-column and inelastic truss elements are employed to accurately model the beam, column, and BRBs. The seismic performance of the BRBFs is evaluated using 91 near-fault pulse-like ground motions with different seismological characteristics, and the maximum inter-storey drift ratio (*MIDR*) and global drift ratio (*GDR*) are recorded as measures of seismic demand. Artificial neural networks (ANNs) are then applied to assess the *MIDR* and *GDR* of the selected prototypes, incorporating ground motion intensity measures as explanatory variables, including amplitude, frequency, and energy content, in addition to structural features. Feature selection techniques are employed to reduce the dimensionality of the high-dimensional data and transform seismological and engineering features into a reduced set of dimensions. The model's bias is checked through residual analysis, while the model's accuracy is evaluated separately using a predictive performance metric, namely, the coefficient of determination, for the training and test datasets. Lastly, the results are assessed by comparing them to the observed trend in the real dataset.

2. Ground Motion Dataset

A total of 91 near-fault pulse-like ground motions from the study of Baker [36] are employed to perform nonlinear dynamic analyses. Baker [36] detected pulse-like ground

motions from non-pulse ones by wavelet analysis and extracted the velocity pulses, in which the pulse indicator (PI) is defined as below:

$$PI = \frac{1}{1 + e^{(-23.3+14.6(PGV \text{ ratio})+20.5(\text{energy ratio}))}} \quad (1)$$

where the *PGV* ratio is the peak ground velocity ratio (*PGV*) of the residual part of motion after pulse extraction to the *PGV* of the original record. In the same way, the energy ratio is described as the energy of the residual record divided by the energy of the original record. The records with *PI* values over 0.85 are classified in the pulse-like ground motion class.

A summary of the key parameters for the selected pulse-wise 91 records, including moment magnitude (M_w), closest distance (R_{clos}), epicentral distance (R_{epi}), pulse period (T_p), peak ground acceleration (*PGA*), *PGV*, and the ratio of *PGA* to *PGV* (*PGA/PGV*), is given in Table A1, Appendix A. These records are obtained from 23 worldwide events with M_w ranging from 5.0 to 7.6, recorded at stations located between 2.5 km and 151.7 km from the epicentre. Figure 1 presents the distribution of ground motion parameters, including M_w versus R_{epi} , *PGA/PGV* versus *PGA*, and T_p versus *PGV*, for the selected records. The selected records encompass a broad spectrum of magnitude, distance, and ground motion parameters, indicating a clear diversity in their characteristics. The records exhibit *PGA* and *PGV* values ranging from 0.1 g to 1.4 g and 30.4 cm/s to 191.1 cm/s, respectively. T_p spans from 0.4 s to 12.9 s, while *PGA/PGV* falls within the range of 0.18 g.s/m to 2.10 g.s/m.

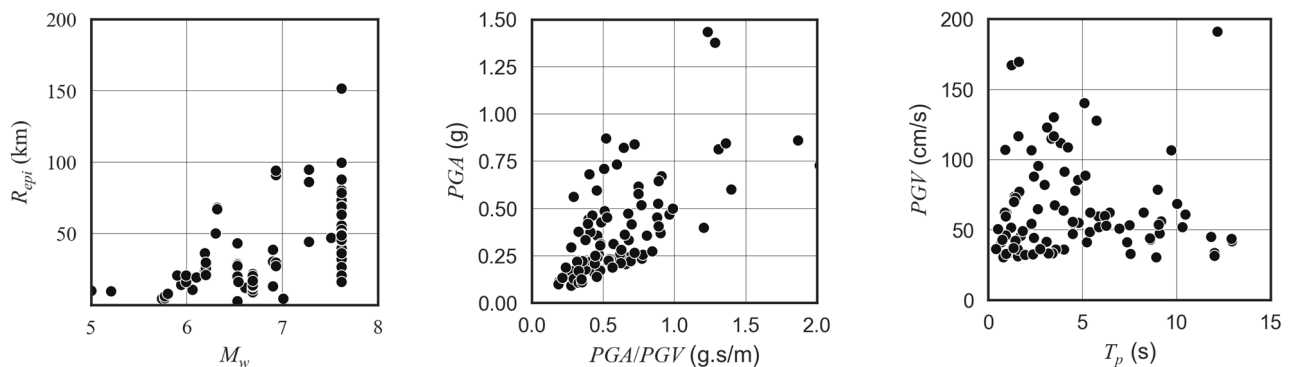


Figure 1. Variation of ground motion parameters for the selected records.

Subsequently, the gathered records are employed to conduct nonlinear time history analyses on twenty-four specific Buckling-Restrained Braced Frames (BRBFs), with detailed findings presented in the subsequent section.

3. Numerical Simulations of the Building Prototypes

The prototype BRBFs designed by Vafaei and Eskandari [37] are remodelled herein. Mega-configured BRBFs with 4, 8, 12, and 15 stories and four bays are designed according to the seismic provisions of the AISC 2005 [38] and Steel Tips 2004 [39] recommendations. The elevation and plan view of the studied BRBFs are provided in Figure 2. The inter-storey height and bay length of the considered BRBFs are 3.2 m and 6 m, respectively. BRBFs are assumed to be located in Los Angeles on stiff soil type (class D) with a distance of 5 km from an active fault, so the near-fault provisions of the Uniform Building Code (UBC 1997) [40] are considered in their design. The importance factor, response modification coefficient, and deflection amplification factor of frames are assumed to be $I = 1$, $R = 7$, and $C_d = 5.5$, respectively, with non-moment-resisting beam-column connections. According to the Coy (2007) [41] study, a connection of beams and braces to the columns is considered to be pinned, which is shown in Figure 3. In the present study, the connection of the beam to the column is modelled with the equal DOF command on the OpenSees platform. Base connections are fully pinned.

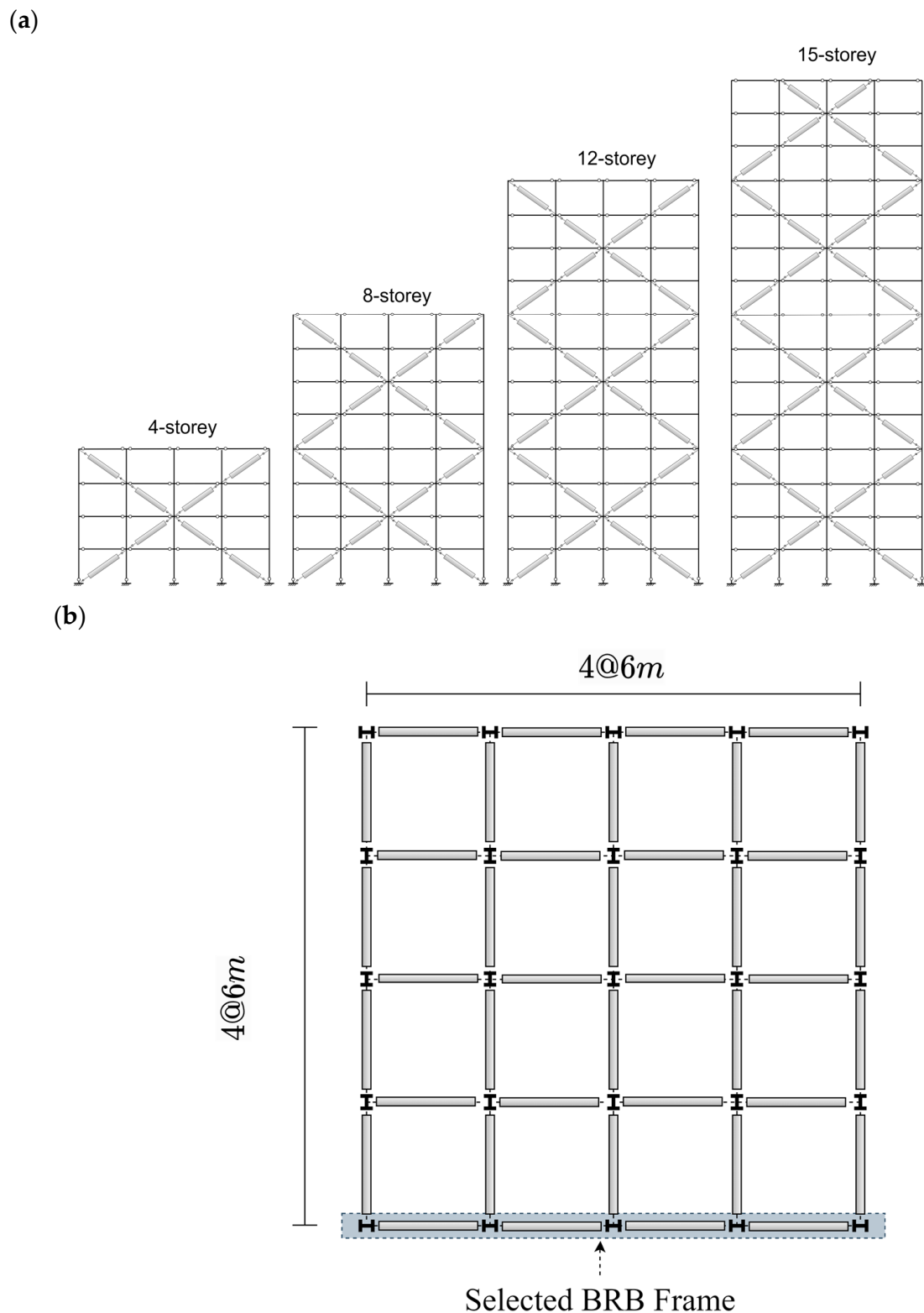


Figure 2. (a) Prototype BRBFs configuration; (b) plan of selected BRBFs.

At the level of the stories, the dead and live loads are 4.7 kN/m^2 and 2.0 kN/m^2 , respectively, whereas at the roof level, these values are 4.0 kN/m^2 and 1.5 kN/m^2 , respectively, following the same sequence. Information on the dimensions of column and beam sections and the core area of BRBs is available in Table A2, Appendix A.

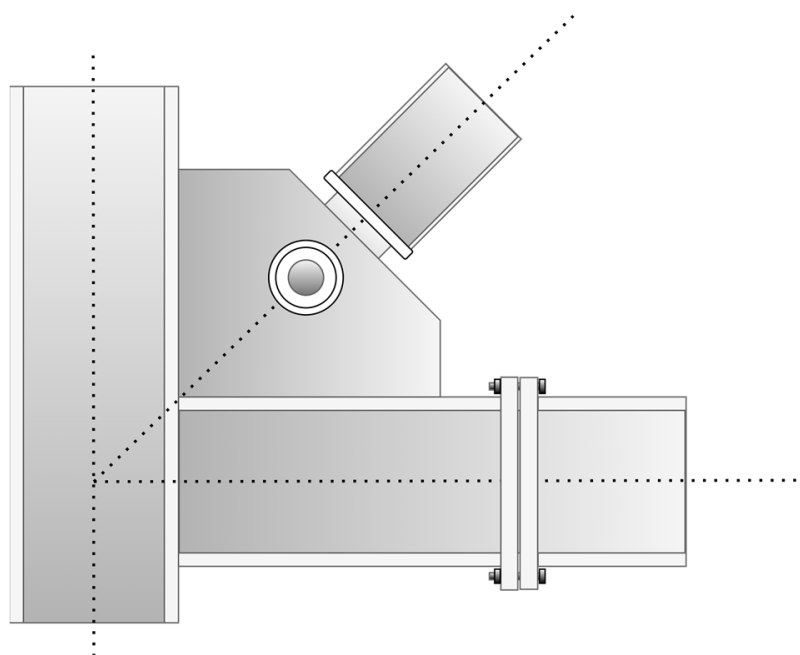


Figure 3. View of beam-column-brace connection (the figure is adapted from Coy [41]).

Numerical simulations of prototype structures are developed on the OpenSees platform. The nonlinear force-beam-column element is considered for beam and column members with distributed plasticity. The cross-section of these members is divided into 20 fibres for each flange and 20 fibres for the web. The BRBs are modelled with inelastic truss elements. To define the materials of the beam and column, Steel01 with a kinematic strain hardening of 2% and elastic moduli (E) ranging from 190 GPa to 215 GPa with increments of 5 GPa are considered. Steel02 material with the given properties in Table 1, an improved version of the Giuffre–Menegotto–Pinto model, is allocated to the bracing members. To assign a maximum ductility of 15 for BRBs, MinMax material with a respective minimum and maximum strain capacity of -0.01467 and 0.01467 is utilised. The isotropic hardening parameters of steel02 are calibrated with the hysteresis behaviour of BRBs in specimen No. 99-1 of the PEER Report 2002/08 [42]. The SAC basic loading history and the SAC near-field loading history are the two protocols [43] to which the specimen is subjected. For example, the comparison of hysteretic curves of experimental and numerical specimens under two loading protocols for Steel02 material with an effective elasticity modulus (which is obtained based on $E = 200$ MPa) is shown in Figure 4. The strain hardening of BRBs is 0.5%. The effective elastic moduli are assumed to overcome the difficulty of modelling BRBs due to the unequal cross-sectional area [37]. An initial imperfection of $1/800$ is set for the buckling of columns. 50% of the total building mass is dedicated to the main nodes of frames. Rayleigh damping ratios of 3%, 4%, 5%, 6%, and 7% are adopted for nonlinear analysis in structural modelling. The periods of the first modes (T) of the studied structures according to the E are presented in Table 2.

Table 1. Steel02 material properties.

| f_y (MPa) | E (GPa) | b | R_0 | CR_1 | CR_2 | a_1 | a_2 | a_3 | a_4 |
|-------------|-----------|-------|-------|--------|--------|--------|-------|--------|-------|
| 290 | 296–335 | 0.005 | 10 | 0.8 | 0.15 | 0.0005 | 0.01 | 0.0005 | 0.01 |

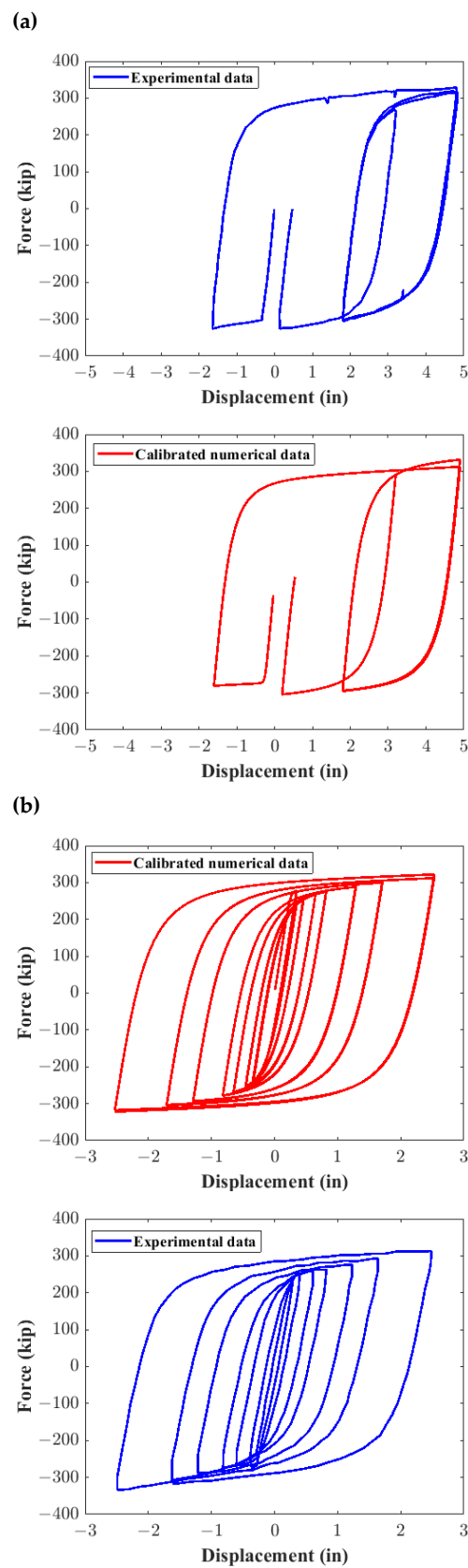


Figure 4. Calibration of Steel02 material using PEER Report 2002/08 [42]. The experimental model and finite element model of BRB with Steel02 material are subjected to two loading protocol sets: (a) the SAC basic loading protocol and (b) the SAC near-field loading protocol.

Table 2. First-mode periods of structures.

| Structure | <i>E</i> (MPa) | 190 | 195 | 200 | 205 | 210 | 215 |
|-----------|----------------|--------|--------|---------|--------|--------|--------|
| | 4-Storey | | 0.55 s | 0.54 s | 0.53 s | 0.53 s | 0.52 s |
| 8-Storey | | 0.79 s | 0.78 s | 0.77 s | 0.76 s | 0.75 s | 0.74 s |
| 12-Storey | | 1.12 s | 1.1 s | 1.089 s | 1.08 s | 1.06 s | 1.05 s |
| 15-Storey | | 1.34 s | 1.32 s | 1.3 s | 1.29 s | 1.27 s | 1.26 s |

Finally, the benchmark input, as detailed by Yaghmaei-Sabegh et al. (2023) [44], adheres to engineering design codes. This study makes minor adjustments to certain parameters to account for uncertainties. Eigenvalue analysis determines the periods of 4, 8, 12, and 15-storey BRBFs with an elastic modulus of 200 MPa, which serve as our benchmark structures. These buildings exhibit periods of 0.53 s, 0.77 s, 1.089 s, and 1.3 s, respectively. Furthermore, more simulations were conducted by varying the elastic modulus within the range of 190 MPa to 215 MPa. The results indicate that the period of the frames changed by less than 5%, which is also less than 0.05 s when compared to the benchmark buildings.

4. Artificial Neural Networks

Artificial neural networks (ANNs) have gained significant popularity in recent years due to their ability to model complex relationships in data with higher degrees of non-linearity effectively. Among them, the Multilayer Perceptron (MLP) is a widely used feedforward neural network consisting of multiple layers of interconnected artificial neurons or nodes [45]. In this study, an MLP from the scikit-learn library is employed to train an ANN-based model for predicting *MIDR* and *GDR*. The scikit-learn library [46] provides a flexible and user-friendly implementation of MLP, allowing us to define the number of hidden layers, number of nodes at each layer, activation function, and much more. A one-layer MLP architecture is constructed (as seen in Figure 5). The input layer of this model consists of representative seismological and structural characteristics. In the subsequent section, the selection of these parameters is detailed, emphasising the assignment of weights that accurately represent the relative importance of the features. The number of nodes within the hidden layer is determined based on empirical testing and optimisation (herein 100 nodes). A rectified linear unit (ReLU) activation function is selected as it was realised to yield the highest prediction performance. This enables the model to effectively learn and represent non-linear relationships within the data. The output layer corresponds to the predicted *MIDR* and *GDR* values. A linear activation function is used in the output layer to produce continuous predictions. Other hyperparameters are appropriately tuned to prevent overfitting or underfitting. Each node in the network receives inputs from the input layer, performs a weighted sum of these inputs using Equation (2), and applies an activation function, given in Equation (3), to produce an output.

$$u_i = \sum_{k=1}^n x_k w_{ik} + b_i \quad (2)$$

$$f(u_i) = \max(0, u_i) \quad (3)$$

In Equation (2), the input signal is represented as x_k , the weighting factors of x_k are denoted as w_{ik} , b_i is a constant value used to shift the activation function, and n and k represent the total number of inputs and index of input, respectively. Additionally, u_i refers to the net output as the linear combination of the weighted inputs and bias. In Equation (3), the function $f(u_i)$ represents the activation function, namely ReLU. This activation function

outputs the input directly if it is positive, and if the input is negative, it outputs zero (the maximum value between 0 and u_i).

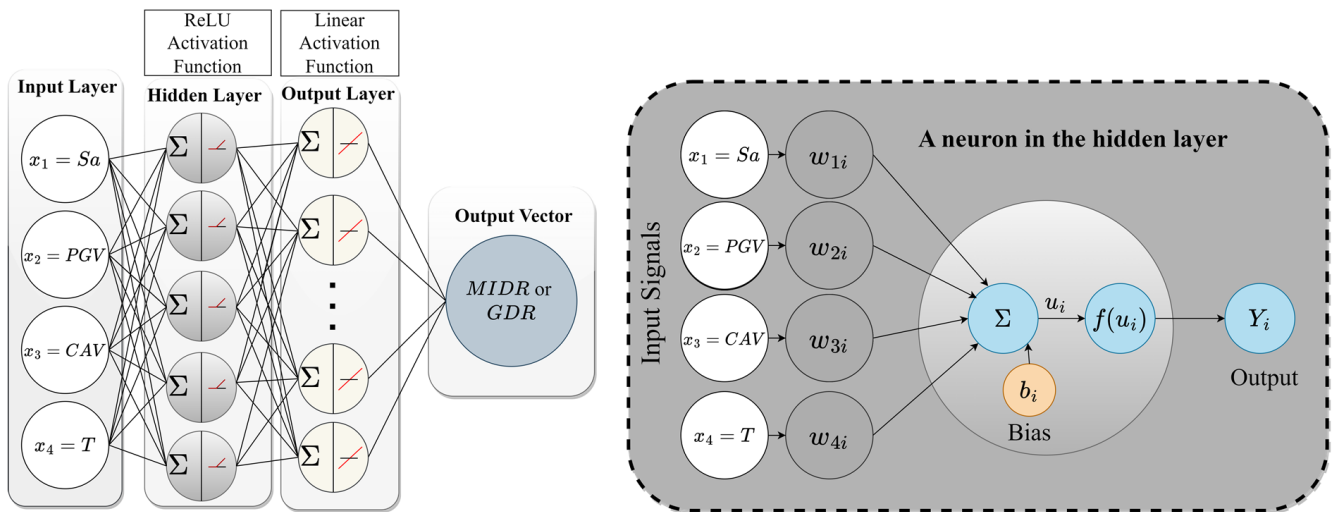


Figure 5. Architecture of the artificial neural network (ANN) model and illustration of artificial neurons of the hidden layer.

5. Results and Discussion

To determine the significance of various input parameters that represent both seismological and structural characteristics in predicting the *MIDR*, this study conducts a feature importance analysis using lightgbm algorithm [47]. The seismological parameters considered are spectral acceleration at the fundamental period of the structure (S_a), *PGA*, *PGV*, *PGA/PGV*, Arias intensity (I_a), cumulative absolute velocity (*CAV*), root mean square acceleration (A_{RMS}), root mean square acceleration (V_{RMS}), and root mean square acceleration (D_{RMS}). Conversely, the structural parameters are the number of stories, T , modulus of elasticity of beam and column (E), modulus of elasticity of BRB (E_{BRB}), yield strength of beam and column, yield strength of BRB, and damping coefficient (ζ). Figure 6 illustrates the arrangement of the most significant parameters for predicting *MIDR* and *GDR*, sorted from the top to the bottom. The findings indicate that the parameter S_a holds the highest importance, whereas E_{BRB} and yield strength in BRBs and in columns and beams have the least significance for both *MIDR* and *GDR*.

It is worth mentioning that, due to multicollinearity between T and the number of stories, only the variable T will be considered for further analysis. To maximise accuracy while minimising the number of input parameters, this study utilises the initial four most crucial parameters, namely *PGA*, *PGV*, S_a , and T (in the case of *MIDR*, *PGV* was used instead of V_{RMS} , which is easier to obtain). However, the analysis indicates that there is no significant difference in the results after adopting each of these two variables. This decision is determined based on extensive experimentation as the input layer for predicting both *MIDR* and *GDR*. Lastly, Figure 7 presents statistical information for both input and output parameters, including minimum (Min), maximum (Max), first quartile (Q1), third quartile (Q3), and mean values for each parameter.

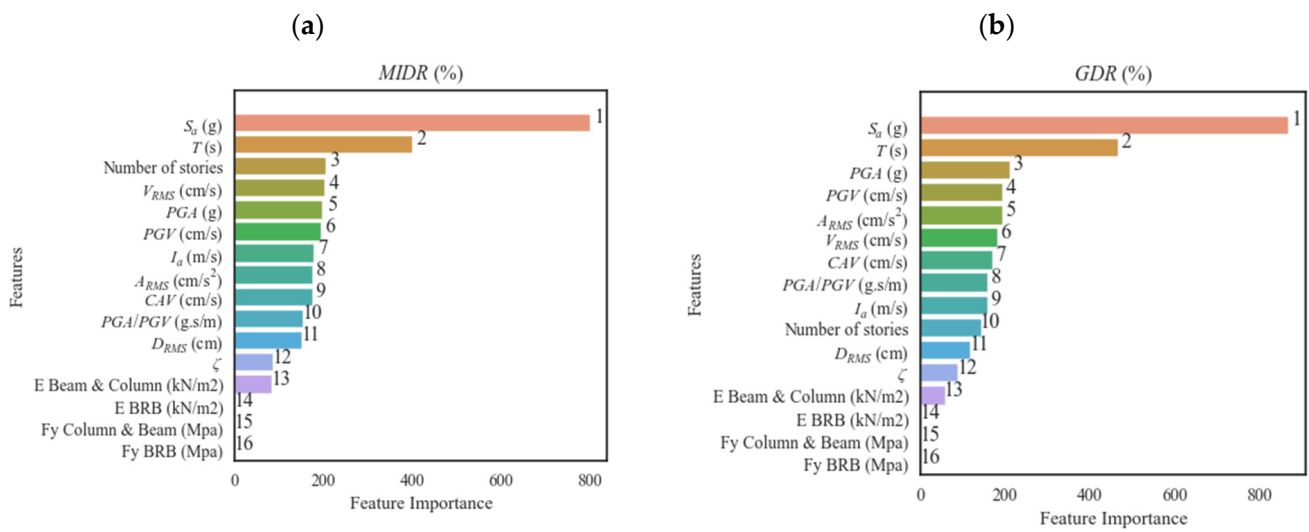


Figure 6. Features important for predicting (a) maximum inter-storey drift ratio (MIDR) and (b) global drift ratio (GDR).

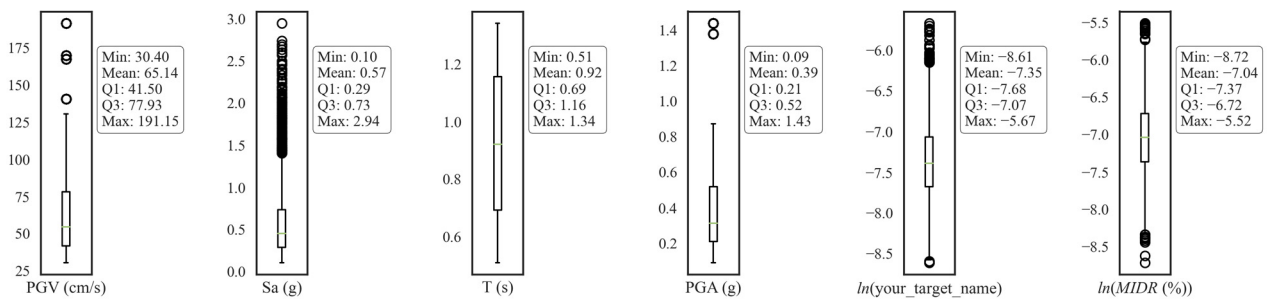


Figure 7. Statistics of the input and output parameters.

Using these parameters, 70% of the dataset is allocated for training purposes, while 30% is reserved for testing and validation. The ANN is utilised to estimate the outputs. Subsequently, the model’s performance is assessed by calculating the coefficient of determination (R^2), Pearson coefficient of correlation (ρ), root mean squared error, and mean absolute percentile error for both the training and testing datasets independently. The obtained results are visualised in Figure 8. It is apparent from the plots that the predictions are highly satisfactory, as they closely align with the ideal fit ($y = x$). The prediction performance of the proposed models is shown in Table 3 for both the training and testing datasets. The results provide statistical evidence supporting the strong performance of these models for both training and test datasets.

Table 3. Prediction performance of the proposed models for global drift ratio (GDR) and maximum inter-storey drift ratio (MIDR).

| Output | Train | | | | Test | | | |
|--------|--------|-------|-------|-------|--------|-------|-------|-------|
| | ρ | RMSE | MAPE | R^2 | ρ | RMSE | MAPE | R^2 |
| MIDR | 0.969 | 0.121 | 0.013 | 0.938 | 0.969 | 0.123 | 0.013 | 0.939 |
| GDR | 0.971 | 0.113 | 0.011 | 0.943 | 0.970 | 0.117 | 0.011 | 0.941 |

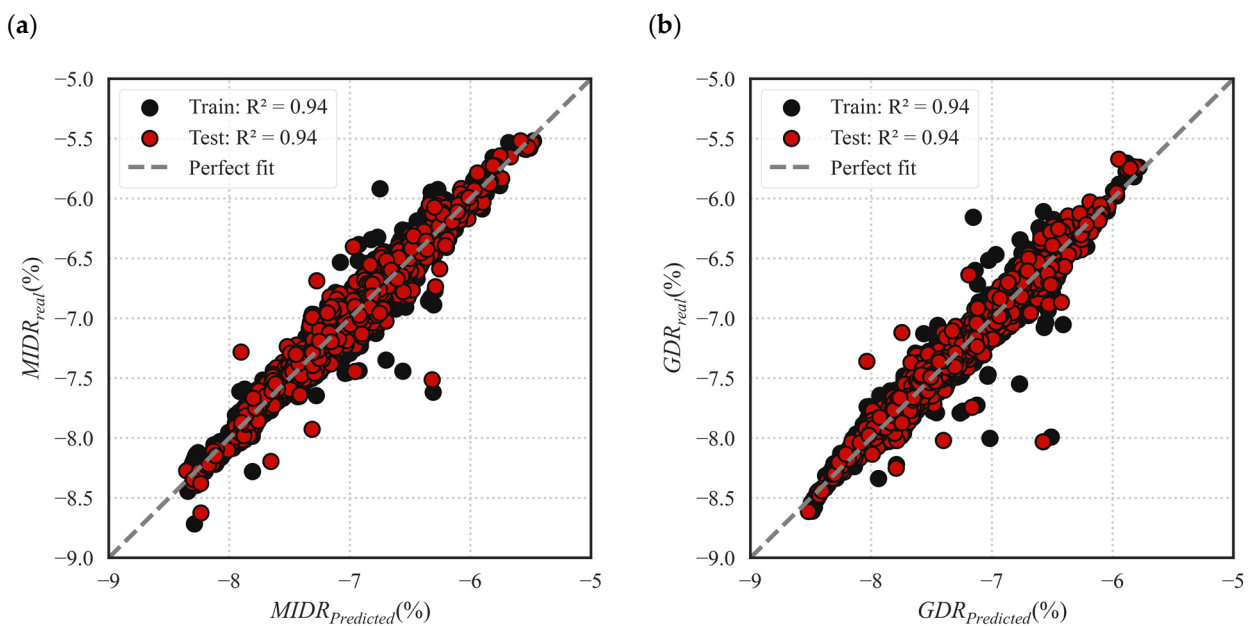


Figure 8. Predicted versus actual values in terms of (a) maximum inter-storey drift ratio (MIDR) and (b) global drift ratio (GDR) for the training and test datasets.

Subsequently, the model's bias is assessed by evaluating the residuals across all values of MIDR and GDR. The residuals are calculated by subtracting the predicted values from the observed values. The results are plotted in Figure 9. The dispersion of residual values for both seismic demand parameters, as depicted, is deemed acceptable, with fluctuations primarily centred around the zero line. Another significant observation is the absence of any notable bias in the predictions in all ranges, indicating the high quality of the predictions and the appropriate selection of parameters for the neural network design for both training and testing data groups.

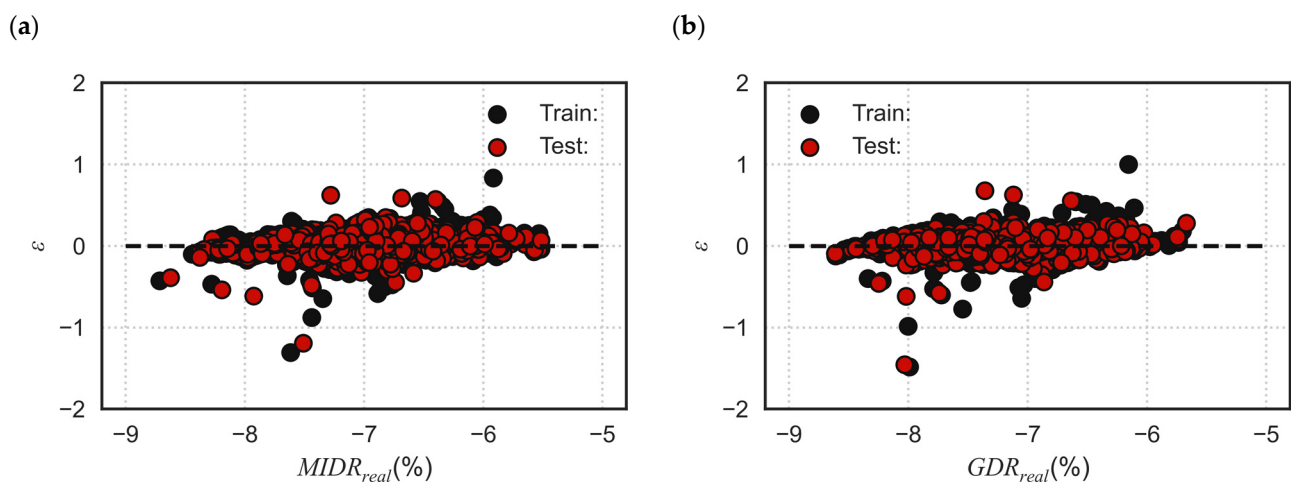


Figure 9. Residuals in terms of (a) maximum inter-storey drift ratio (MIDR) and (b) global drift ratio (GDR) for the training and test datasets.

Additionally, the model error distribution, which is the ratio of values obtained from numerical simulation and the obtained values from surrogate ANN models, is depicted in Figure 10. As clearly visible, the model errors of both GDR and MIDR models have a balanced distribution with a mean of 1.00 and a coefficient of variation of 0.02 in both training and test datasets. However, as evaluated through a null hypothesis test, they do not conform to a particular distribution function.

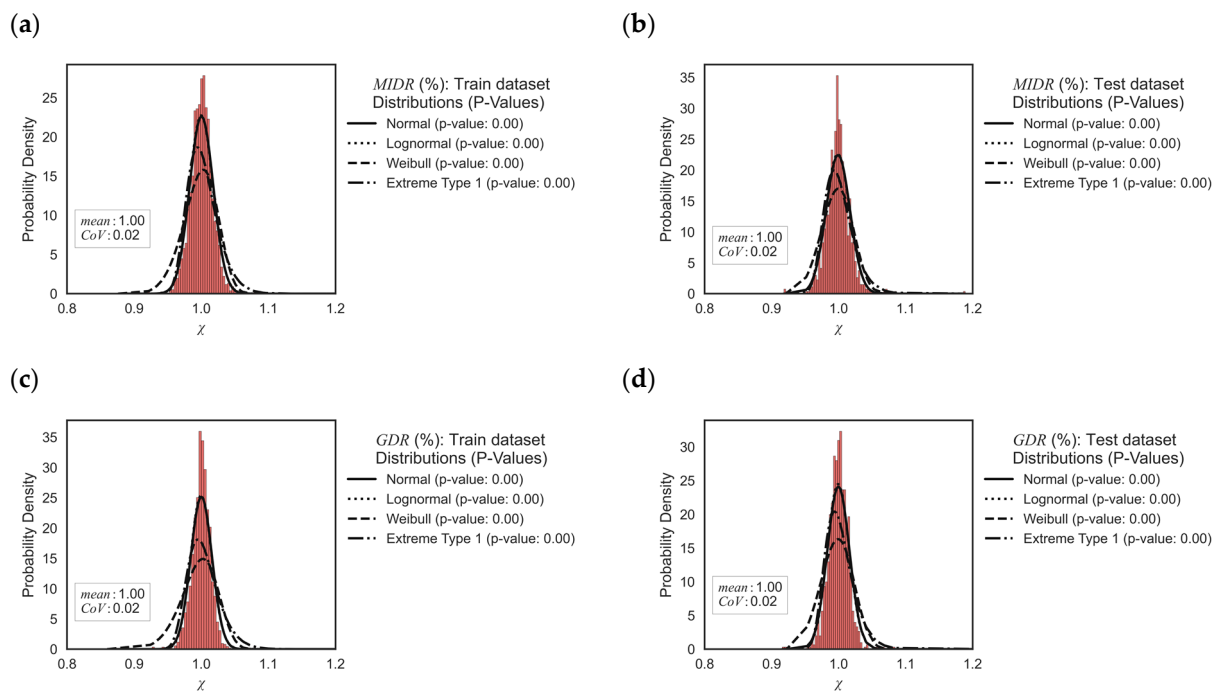


Figure 10. Distribution of model error for (a) MIDR with a training dataset, (b) MIDR with a test dataset, (c) GDR with a training dataset, and (d) GDR with a test dataset.

Figure 11 depicts the correlation between input variables and *MIDR* and *GDR*, utilising real data and model predictions. The results demonstrate similar Pearson correlation coefficient (r) values for both real data and model predictions, which highlights the ability of the model to track the physical behaviour of the problem at hand. It is shown that an increase in all four input parameters will result in a rise in both *GDR* and *MIDR*.

To further analyse our results, we investigate the Shapley additive explanation (SHAP), as introduced in reference [48]. SHAP is a method rooted in game theory that offers a means to interpret the predictions generated by machine learning models, including ANN. The core principle behind SHAP involves generating predictions with and without the inclusion of individual input variables. By comparing these predictions, SHAP quantifies the significance of each input variable in influencing the model's output. Figure 12 presents the SHAP values for the test database alongside the input features of the model for *GDR* and *MIDR*. The x -axis of these graphs displays the SHAP values for each BRBF subjected to each record, while the y -axis presents the input variables arranged in descending order of significance, with the most influential variables at the top and the least influential at the bottom. The colour scale used to represent the values of input variables spans from the lowest (blue) to the highest (red). These plots reveal that the model's outcome is notably impacted by S_a and T_s . As evident from the observations, the models anticipate that an increase in *GDR* and *MIDR* will occur with an increase in each of the parameters. This alignment with the trend depicted in Figure 11 reinforces the consistency between the model's expectations and the observed patterns.

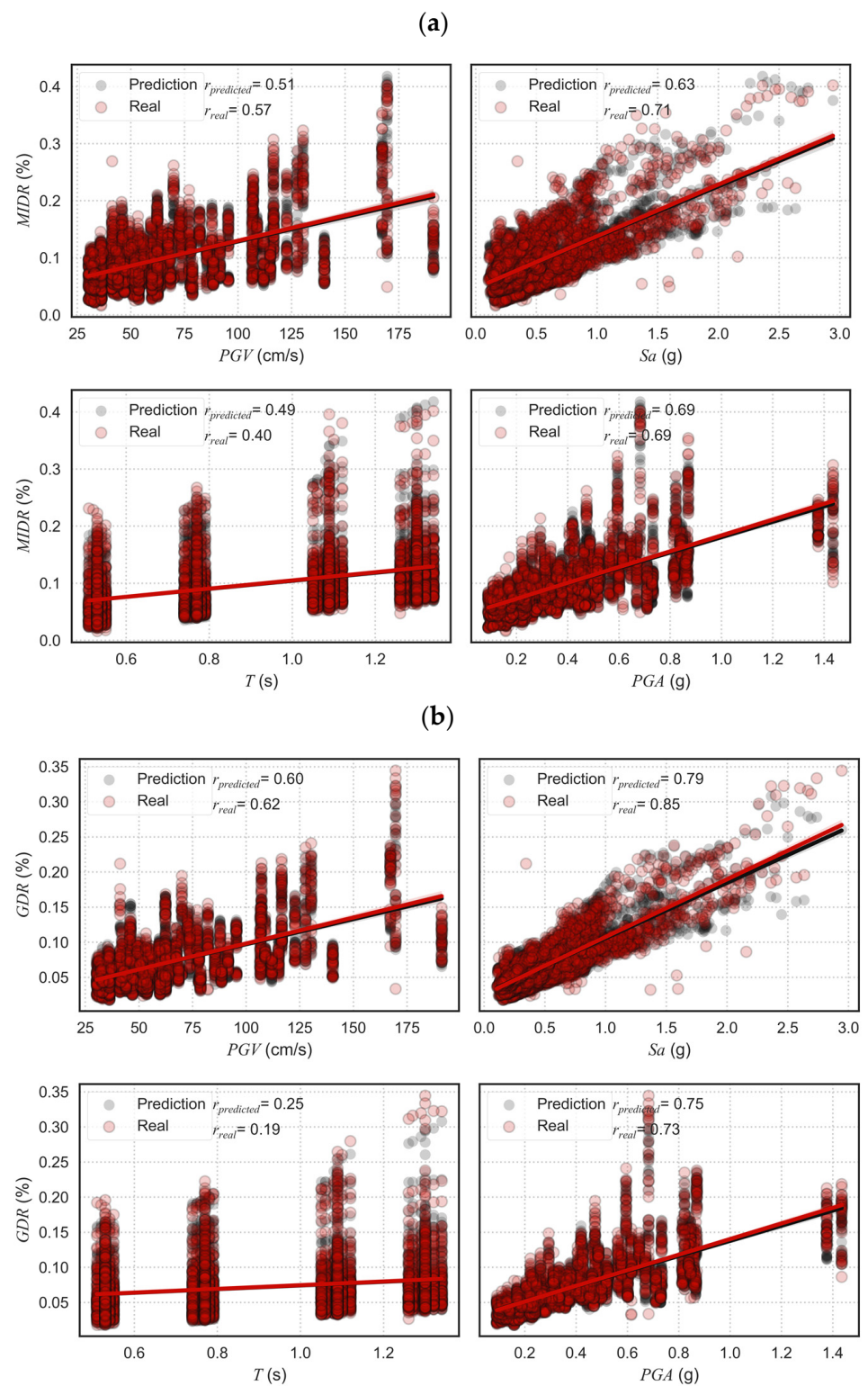


Figure 11. Influence of the input variables on (a) maximum inter-storey drift ratio (MIDR) and (b) global drift ratio (GDR) based on real data and model predictions.

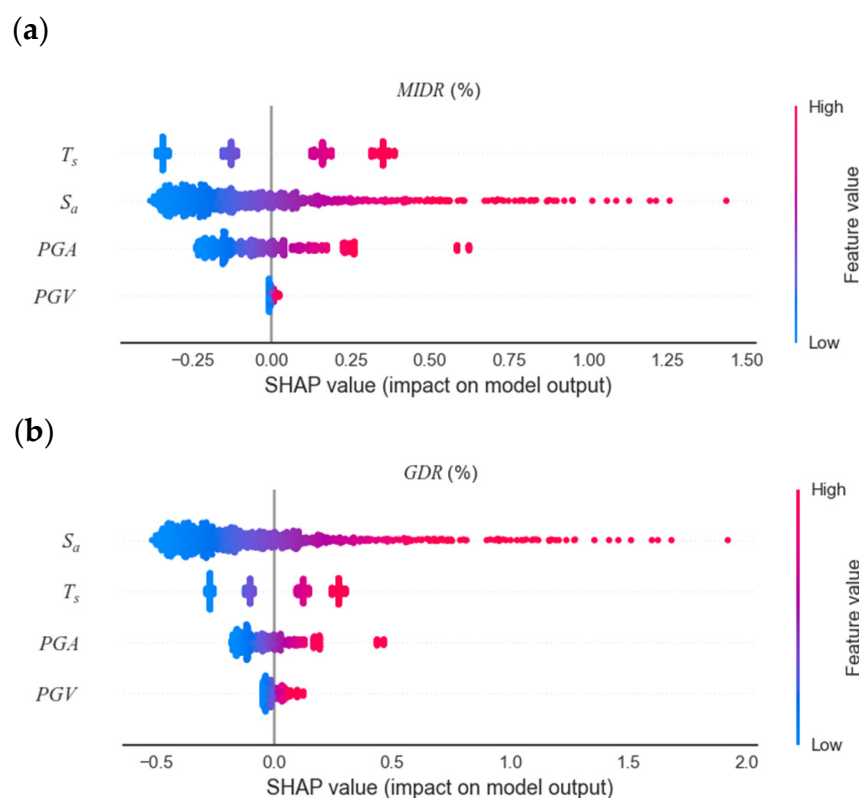


Figure 12. Shapley additive explanation (SHAP) plots of the developed ANN models for (a) maximum inter-storey drift ratio (*MIDR*) and (b) global drift ratio (*GDR*).

It is essential to mention that our benchmark model has been rigorously validated, as previously detailed in Yaghmaei-Sabegh et al. (2023) [44]. Within the context of machine learning, it is worth highlighting that we have dedicated 30% of the dataset to the formation of the test/validation dataset. It is of paramount importance to note that our model aptly mirrors the accuracy observed within the training dataset, affirming its validation against the actual dataset.

Finally, in accordance with the findings presented by Veismoradi and Darvishan (2018) [49], it has been demonstrated that mega-configured BRBFs exhibit commendable performance characteristics when subjected to both pulse-like and non-pulse-like ground motions. Consequently, this configuration emerges as a viable and effective option for enhancing the seismic resilience of BRBFs in the face of near-fault earthquakes. These findings contribute significantly to the potential of mega-configured BRBFs. Therefore, we have followed a general thought in seismic demand predictions based on machine learning methods where the defined models could be used for approximate yet simple demand predictions of BRBFs.

6. Conclusions

This paper presents a novel machine learning-based approach to estimate seismic demands in buckling restrained brace frames (BRBFs), addressing the challenge of compression-induced buckling behaviour. The study develops BRBFs with energy absorption cores and restraining segments, employing various materials. Prototype BRBFs with different properties are modelled using numerical simulations and evaluated using 91 pulse-wise ground motions. An artificial neural network (ANN) is utilised to assess seismic demands in terms of maximum inter-storey drift ratio (*MIDR*) and global drift ratio (*GDR*), incorporating the most representative ground motion intensity measures and structural features. The results are summarised as follows:

- The analysis of feature selection indicates that spectral acceleration on the fundamental period (T) of the structure (S_a), followed by T itself, exhibits the highest level of influence in predicting the seismic demand of BRBFs in terms of both *MIDR* and *GDR*. On the other hand, f_y in buckling restrained braces (BRBs) has the least impact.
- Out of all the considered parameters, in addition to the f_y in BRBs, f_y in the beams and columns, the elastic modulus (E) of the BRBs and beams, E of beams and columns, damping ratio (ζ), as well as the root mean square acceleration (D_{RMS}), rank as the least influential factors impacting the seismic demand of the studied structures in terms of both *MIDR* and *GDR*.
- The results indicate that incorporating *PGA* and *PGV* in addition to S_a and T as input parameters (which are the top important parameters identified through feature selection) leads to enhanced predicted outcomes in terms of performance, unbiasedness, and variability of residuals between predictions and observed values. Notably, a relatively higher coefficient of determination, Pearson coefficient of correlation, and lower error values are observed in both the training and testing datasets, affirming the close correspondence between our predictions and the observed behaviour.
- The dispersion of residual values for the examined seismic demand parameters in this study is considered satisfactory, as most fluctuations are centred around the zero line. Moreover, the lack of any discernible bias in the predictions emphasises the high accuracy of our predictions and the appropriate choice of parameters in the neural network design for both the training and testing datasets.
- Furthermore, the model error distribution, which signifies the relationship between values generated through numerical simulations and those predicted by surrogate ANN models, consistently exhibits a balanced distribution across both the training and test datasets. This balance is evident in the form of a mean value of 1.00 and a coefficient of variation of 0.02. It is noteworthy, however, that statistical analysis via a null hypothesis test reveals that these error distributions do not align with any specific statistical distribution function.
- Furthermore, the outcomes of the Shapley additive explanation (SHAP) analysis demonstrate that S_a and T_s significantly impact the model predictions, corroborating the earlier findings from the feature selection analysis.
- The study provides further insights into the influence of input variables on *MIDR* and *GDR* using real data and model predictions. The findings reveal similar model performance values regarding different metrics for the selected input parameters for both real data and model predictions. This is a sign of the model's capability to truly consider the effects of all input parameters, along with its high accuracy.
- Mega-configured BRBFs have showcased noteworthy performance attributes when exposed to various ground motion types, encompassing both pulse-like and non-pulse-like motions. This configuration stands out as a promising and efficient choice for bolstering the seismic resilience of BRBFs, particularly in the context of near-fault seismic events. These research outcomes significantly enhance the prospects and application of mega-configured BRBFs in seismic engineering. Therefore, this study aligns with the prevailing trend in seismic demand prediction, employing machine learning methodologies to establish models capable of providing simplified yet valuable demand estimates for BRBFs.

Finally, the model presented in this paper offers a valuable tool for the rapid prediction of seismic demand in terms of *MIDR* and *GDR* for BRBFs. However, it should be noted that the results obtained are specific to the investigated prototypes and pulse-wise records. Furthermore, it is noteworthy that the models introduced herein have not undergone comparative evaluation with pre-existing models in the scientific literature. This omission arises due to the unavailability of machine learning-based models specifically designed for the seismic demand estimation of the structures examined in this research. Nevertheless, we acknowledge the necessity for future investigations to build upon this research by encompassing a wider array of building classifications and delving into alternative machine

learning algorithms, including the effect of far-field ground motion records. This will enable a comprehensive assessment of the models introduced in this study.

Author Contributions: A.M.: Conceptualization, Data curation, Formal analysis, Methodology, Validation, Visualization, Writing—review and editing; S.K.: Funding acquisition, Methodology, Project administration, Supervision, Validation, Writing—original draft, Writing—review and editing; S.Y.-S.: Data curation, Methodology, Supervision, Writing—review and editing; M.R.: Formal analysis, Data curation, Methodology, Writing—review and editing; P.B.L.: Funding acquisition, Supervision, Writing—review and editing. All authors have read and agreed to the published version of the manuscript.

Funding: This work was partly financed by FCT/MCTES through national funds (PIDDAC) under the R&D Unit Institute for Sustainability and Innovation in Structural Engineering (ISISE), under reference UIDB/04029/2020, and under the Associate Laboratory Advanced Production and Intelligent Systems ARISE under reference LA/P/0112/2020.

Data Availability Statement: Data supporting the reported results and the web-based application in the present study are available upon request from the corresponding author.

Conflicts of Interest: The authors declare no conflict of interest.

Appendix A

Table A1. Ground motion characteristics.

| No | Event | Year | Station | M_w | R_{clos} (km) | R_{epi} (km) | T_p (s) | PGV (cm/s) | PGA (g) | PGA/PGV (g.s/m) |
|----|-----------------------|------|----------------------------------|-------|--------------------|-------------------|--------------|---------------|------------|--------------------|
| 1 | San Fernando | 1971 | Pacoima Dam (upper left abut) | 6.6 | 1.8 | 11.9 | 1.6 | 116.5 | 1.4 | 1.23 |
| 2 | Coyote Lake | 1979 | Gilroy Array #6 | 5.7 | 3.1 | 4.4 | 1.2 | 51.5 | 0.5 | 0.88 |
| 3 | Imperial Valley-06 | 1979 | Aeropuerto Mexicali | 6.5 | 0.3 | 2.5 | 2.4 | 44.3 | 0.4 | 0.81 |
| 4 | Imperial Valley-06 | 1979 | Agrarias | 6.5 | 0.7 | 2.6 | 2.3 | 54.4 | 0.3 | 0.57 |
| 5 | Imperial Valley-06 | 1979 | Brawley Airport | 6.5 | 10.4 | 43.2 | 4 | 36.1 | 0.2 | 0.44 |
| 6 | Imperial Valley-06 | 1979 | EC County Center FF | 6.5 | 7.3 | 29.1 | 4.5 | 54.5 | 0.2 | 0.33 |
| 7 | Imperial Valley-06 | 1979 | EC Meloland Overpass FF | 6.5 | 0.1 | 19.4 | 3.3 | 115 | 0.4 | 0.33 |
| 8 | Imperial Valley-06 | 1979 | El Centro Array #10 | 6.5 | 6.2 | 26.3 | 4.5 | 46.9 | 0.2 | 0.38 |
| 9 | Imperial Valley-06 | 1979 | El Centro Array #11 | 6.5 | 12.5 | 29.4 | 7.4 | 41.1 | 0.4 | 0.90 |
| 10 | Imperial Valley-06 | 1979 | El Centro Array #3 | 6.5 | 12.9 | 28.7 | 5.2 | 41.1 | 0.2 | 0.56 |
| 11 | Imperial Valley-06 | 1979 | El Centro Array #4 | 6.5 | 7.1 | 27.1 | 4.6 | 77.9 | 0.4 | 0.46 |
| 12 | Imperial Valley-06 | 1979 | El Centro Array #5 | 6.5 | 4 | 27.8 | 4 | 91.5 | 0.4 | 0.41 |
| 13 | Imperial Valley-06 | 1979 | El Centro Array #6 | 6.5 | 1.4 | 27.5 | 3.8 | 111.9 | 0.4 | 0.39 |
| 14 | Imperial Valley-06 | 1979 | El Centro Array #7 | 6.5 | 0.6 | 27.6 | 4.2 | 108.8 | 0.5 | 0.42 |

Table A1. Cont.

| No | Event | Year | Station | M_w | R_{clos} (km) | R_{epi} (km) | T_p (s) | PGV (cm/s) | PGA (g) | PGA/PGV (g.s/m) |
|----|-----------------------|------|-------------------------------|-------|--------------------|-------------------|--------------|---------------|------------|--------------------|
| 15 | Imperial Valley-06 | 1979 | El Centro Array #8 | 6.5 | 3.9 | 28.1 | 5.4 | 48.6 | 0.5 | 0.96 |
| 16 | Imperial Valley-06 | 1979 | El Centro Differential Array | 6.5 | 5.1 | 27.2 | 5.9 | 59.6 | 0.4 | 0.70 |
| 17 | Imperial Valley-06 | 1979 | Holtville Post Office | 6.5 | 7.7 | 19.8 | 4.8 | 55.1 | 0.3 | 0.47 |
| 18 | Mammoth Lakes-06 | 1980 | Long Valley Dam (Upr L Abut) | 5.9 | | 14 | 1.1 | 33.1 | 0.4 | 1.21 |
| 19 | Irpinia, Italy-01 | 1980 | Sturno | 6.9 | 10.8 | 30.4 | 3.1 | 41.5 | 0.2 | 0.56 |
| 20 | Westmorland | 1981 | Parachute Test Site | 5.9 | 16.7 | 20.5 | 3.6 | 35.8 | 0.2 | 0.48 |
| 21 | Coalinga-05 | 1983 | Oil City | 5.8 | | 4.6 | 0.7 | 41.2 | 0.9 | 2.10 |
| 22 | Coalinga-05 | 1983 | Transmitter Hill | 5.8 | | 6 | 0.9 | 46.1 | 0.9 | 1.87 |
| 23 | Coalinga-07 | 1983 | Coalinga-14th & Elm (Old CHP) | 5.2 | | 9.6 | 0.4 | 36.1 | 0.7 | 2.02 |
| 24 | Morgan Hill | 1984 | Coyote Lake Dam (SW Abut) | 6.2 | 0.5 | 24.6 | 1 | 62.3 | 0.8 | 1.31 |
| 25 | Morgan Hill | 1984 | Gilroy Array #6 | 6.2 | 9.9 | 36.3 | 1.2 | 35.4 | 0.2 | 0.69 |
| 26 | Taiwan SMART1(40) | 1986 | SMART1 C00 | 6.3 | | 68.2 | 1.6 | 31.2 | 0.2 | 0.66 |
| 27 | Taiwan SMART1(40) | 1986 | SMART1 M07 | 6.3 | | 67.2 | 1.6 | 36.1 | 0.2 | 0.64 |
| 28 | N. Palm Springs | 1986 | North Palm Springs | 6.1 | 4 | 10.6 | 1.4 | 73.6 | 0.7 | 0.91 |
| 29 | San Salvador | 1986 | GeotechInvestigCenter | 5.8 | 6.3 | 7.9 | 0.9 | 62.3 | 0.8 | 1.36 |
| 30 | Whittier Narrows-01 | 1987 | Downey—Co MaintBldg | 6 | 20.8 | 16 | 0.8 | 30.4 | 0.2 | 0.77 |
| 31 | Whittier Narrows-01 | 1987 | LB—Orange Ave | 6 | 24.5 | 20.7 | 1 | 32.9 | 0.3 | 0.78 |
| 32 | Superstition Hills-02 | 1987 | Parachute Test Site | 6.5 | 1 | 16 | 2.3 | 106.8 | 0.4 | 0.39 |
| 33 | Loma Prieta | 1989 | Alameda Naval Air Stn Hanger | 6.9 | 71 | 90.8 | 2 | 32.2 | 0.2 | 0.69 |
| 34 | Loma Prieta | 1989 | Gilroy Array #2 | 6.9 | 11.1 | 29.8 | 1.7 | 45.7 | 0.4 | 0.89 |
| 35 | Loma Prieta | 1989 | Oakland—Outer Harbor Wharf | 6.9 | 74.3 | 94 | 1.8 | 49.2 | 0.3 | 0.68 |
| 36 | Loma Prieta | 1989 | Saratoga—Aloha Ave | 6.9 | 8.5 | 27.2 | 4.5 | 55.6 | 0.4 | 0.65 |
| 37 | Erzican, Turkey | 1992 | Erzincan | 6.7 | 4.4 | 9 | 2.7 | 95.4 | 0.5 | 0.51 |
| 38 | Cape Mendocino | 1992 | Petrolia | 7 | 8.2 | 4.5 | 3 | 82.1 | 0.6 | 0.75 |
| 39 | Landers | 1992 | Barstow | 7.3 | 34.9 | 94.8 | 8.9 | 30.4 | 0.1 | 0.45 |
| 40 | Landers | 1992 | Lucerne | 7.3 | 2.2 | 44 | 5.1 | 140.3 | 0.7 | 0.51 |
| 41 | Landers | 1992 | Yermo Fire Station | 7.3 | 23.6 | 86 | 7.5 | 53.2 | 0.2 | 0.42 |
| 42 | Northridge-01 | 1994 | Jensen Filter Plant | 6.7 | 5.4 | 13 | 3.5 | 67.4 | 0.5 | 0.77 |

Table A1. Cont.

| No | Event | Year | Station | M_w | R_{clos} (km) | R_{epi} (km) | T_p (s) | PGV (cm/s) | PGA (g) | PGA/PGV (g.s/m) |
|----|--------------------|------|-----------------------------------|-------|--------------------|-------------------|--------------|---------------|------------|--------------------|
| 43 | Northridge-01 | 1994 | Jensen Filter Plant Generator | 6.7 | 5.4 | 13 | 3.5 | 67.4 | 0.5 | 0.77 |
| 44 | Northridge-01 | 1994 | LA—Wadsworth VA Hospital North | 6.7 | 23.6 | 19.6 | 2.4 | 32.4 | 0.3 | 0.85 |
| 45 | Northridge-01 | 1994 | LA Dam | 6.7 | 5.9 | 11.8 | 1.7 | 77.1 | 0.6 | 0.75 |
| 46 | Northridge-01 | 1994 | Newhall—W Pico Canyon Rd. | 6.7 | 5.5 | 21.6 | 2.4 | 87.8 | 0.4 | 0.49 |
| 47 | Northridge-01 | 1994 | Pacoima Dam (downstr) | 6.7 | 7 | 20.4 | 0.5 | 50.4 | 0.5 | 0.99 |
| 48 | Northridge-01 | 1994 | Pacoima Dam (upper left) | 6.7 | 7 | 20.4 | 0.9 | 107.1 | 1.4 | 1.29 |
| 49 | Northridge-01 | 1994 | Rinaldi Receiving Sta | 6.7 | 6.5 | 10.9 | 1.2 | 167.2 | 0.9 | 0.52 |
| 50 | Northridge-01 | 1994 | Sylmar—Converter Sta | 6.7 | 5.4 | 13.1 | 3.5 | 130.3 | 0.6 | 0.46 |
| 51 | Northridge-01 | 1994 | Sylmar—Converter Sta East | 6.7 | 5.2 | 13.6 | 3.5 | 116.6 | 0.8 | 0.72 |
| 52 | Northridge-01 | 1994 | Sylmar—Olive View Med FF | 6.7 | 5.3 | 16.8 | 3.1 | 122.7 | 0.7 | 0.60 |
| 53 | Kobe, Japan | 1995 | Takarazuka | 6.9 | 0.3 | 38.6 | 1.4 | 72.6 | 0.6 | 0.89 |
| 54 | Kobe, Japan | 1995 | Takatori | 6.9 | 1.5 | 13.1 | 1.6 | 169.6 | 0.7 | 0.40 |
| 55 | Kocaeli, Turkey | 1999 | Gebze | 7.5 | 10.9 | 47 | 5.9 | 52 | 0.2 | 0.46 |
| 56 | Chi-Chi, Taiwan | 1999 | CHY006 | 7.6 | 9.8 | 40.5 | 2.6 | 64.7 | 0.3 | 0.48 |
| 57 | Chi-Chi, Taiwan | 1999 | CHY035 | 7.6 | 12.7 | 43.9 | 1.4 | 42 | 0.3 | 0.62 |
| 58 | Chi-Chi, Taiwan | 1999 | CHY101 | 7.6 | 10 | 32 | 4.8 | 85.4 | 0.5 | 0.53 |
| 59 | Chi-Chi, Taiwan | 1999 | TAP003 | 7.6 | 102.4 | 151.7 | 3.4 | 33 | 0.1 | 0.28 |
| 60 | Chi-Chi, Taiwan | 1999 | TCU029 | 7.6 | 28.1 | 79.2 | 6.4 | 62.3 | 0.2 | 0.35 |
| 61 | Chi-Chi, Taiwan | 1999 | TCU031 | 7.6 | 30.2 | 80.1 | 6.2 | 59.9 | 0.1 | 0.19 |
| 62 | Chi-Chi, Taiwan | 1999 | TCU034 | 7.6 | 35.7 | 87.9 | 8.6 | 42.8 | 0.2 | 0.54 |
| 63 | Chi-Chi, Taiwan | 1999 | TCU036 | 7.6 | 19.8 | 67.8 | 5.4 | 62.4 | 0.1 | 0.22 |
| 64 | Chi-Chi, Taiwan | 1999 | TCU038 | 7.6 | 25.4 | 73.1 | 7 | 50.9 | 0.1 | 0.28 |
| 65 | Chi-Chi, Taiwan | 1999 | TCU040 | 7.6 | 22.1 | 69 | 6.3 | 53 | 0.1 | 0.27 |
| 66 | Chi-Chi, Taiwan | 1999 | TCU042 | 7.6 | 26.3 | 78.4 | 9.1 | 47.3 | 0.2 | 0.44 |
| 67 | Chi-Chi, Taiwan | 1999 | TCU046 | 7.6 | 16.7 | 68.9 | 8.6 | 44 | 0.1 | 0.32 |
| 68 | Chi-Chi, Taiwan | 1999 | TCU049 | 7.6 | 3.8 | 38.9 | 11.8 | 44.8 | 0.3 | 0.63 |

Table A1. Cont.

| No | Event | Year | Station | M_w | R_{clos} (km) | R_{epi} (km) | T_p (s) | PGV (cm/s) | PGA (g) | PGA/PGV (g.s/m) |
|----|-----------------------|------|----------------------|-------|--------------------|-------------------|--------------|---------------|------------|--------------------|
| 69 | Chi-Chi, Taiwan | 1999 | TCU053 | 7.6 | 6 | 41.2 | 12.9 | 41.9 | 0.2 | 0.54 |
| 70 | Chi-Chi, Taiwan | 1999 | TCU054 | 7.6 | 5.3 | 37.6 | 10.5 | 60.9 | 0.2 | 0.28 |
| 71 | Chi-Chi, Taiwan | 1999 | TCU056 | 7.6 | 10.5 | 39.7 | 12.9 | 43.5 | 0.1 | 0.29 |
| 72 | Chi-Chi, Taiwan | 1999 | TCU060 | 7.6 | 8.5 | 45.4 | 12 | 33.7 | 0.2 | 0.62 |
| 73 | Chi-Chi, Taiwan | 1999 | TCU065 | 7.6 | 0.6 | 26.7 | 5.7 | 127.7 | 0.8 | 0.64 |
| 74 | Chi-Chi, Taiwan | 1999 | TCU068 | 7.6 | 0.3 | 47.9 | 12.2 | 191.1 | 0.6 | 0.29 |
| 75 | Chi-Chi, Taiwan | 1999 | TCU075 | 7.6 | 0.9 | 20.7 | 5.1 | 88.4 | 0.3 | 0.38 |
| 76 | Chi-Chi, Taiwan | 1999 | TCU076 | 7.6 | 2.8 | 16 | 4 | 63.7 | 0.3 | 0.48 |
| 77 | Chi-Chi, Taiwan | 1999 | TCU082 | 7.6 | 5.2 | 36.2 | 9.2 | 56.1 | 0.2 | 0.44 |
| 78 | Chi-Chi, Taiwan | 1999 | TCU087 | 7.6 | 7 | 55.6 | 9 | 53.7 | 0.1 | 0.18 |
| 79 | Chi-Chi, Taiwan | 1999 | TCU098 | 7.6 | 47.7 | 99.7 | 7.5 | 32.7 | 0.1 | 0.33 |
| 80 | Chi-Chi, Taiwan | 1999 | TCU101 | 7.6 | 2.1 | 45.1 | 10 | 68.4 | 0.2 | 0.32 |
| 81 | Chi-Chi, Taiwan | 1999 | TCU102 | 7.6 | 1.5 | 45.6 | 9.7 | 106.6 | 0.3 | 0.27 |
| 82 | Chi-Chi, Taiwan | 1999 | TCU103 | 7.6 | 6.1 | 52.4 | 8.3 | 62.2 | 0.1 | 0.21 |
| 83 | Chi-Chi, Taiwan | 1999 | TCU104 | 7.6 | 12.9 | 49.3 | 12 | 31.4 | 0.1 | 0.35 |
| 84 | Chi-Chi, Taiwan | 1999 | TCU128 | 7.6 | 13.2 | 63.3 | 9 | 78.7 | 0.2 | 0.24 |
| 85 | Chi-Chi, Taiwan | 1999 | TCU136 | 7.6 | 8.3 | 48.8 | 10.3 | 51.8 | 0.2 | 0.33 |
| 86 | Northwest China-03 | 1997 | Jiashi | 6.1 | | 19.1 | 1.3 | 37 | 0.3 | 0.72 |
| 87 | Yountville | 2000 | Napa Fire Station #3 | 5 | | 9.9 | 0.7 | 43 | 0.6 | 1.40 |
| 88 | Chi-Chi, Taiwan-03 | 1999 | CHY024 | 6.2 | 19.7 | 25.5 | 3.2 | 33.1 | 0.2 | 0.56 |
| 89 | Chi-Chi, Taiwan-03 | 1999 | CHY080 | 6.2 | 22.4 | 29.5 | 1.4 | 69.9 | 0.5 | 0.68 |
| 90 | Chi-Chi, Taiwan-03 | 1999 | TCU076 | 6.2 | 14.7 | 20.8 | 0.9 | 59.4 | 0.5 | 0.88 |
| 91 | Chi-Chi, Taiwan-06 | 1999 | CHY101 | 6.3 | 36 | 50 | 2.8 | 36.3 | 0.1 | 0.35 |

Table A2. Dimensions of columns, beams, and BRBs.

| Stories | Exterior Column | Interior Column | Beam | Cross Section Area of Brace (cm ²) |
|----------------|-----------------|-----------------|----------|--|
| 4-Storey BRBF | | | | |
| 1 | W14 × 38 | W14 × 38 | W12 × 19 | 29.23 |
| 2 | W14 × 38 | W14 × 38 | W12 × 19 | 24.62 |
| 3 | W14 × 26 | W14 × 26 | W12 × 19 | 18.46 |
| 4 | W14 × 26 | W14 × 26 | W12 × 19 | 13.85 |
| 8-Storey BRBF | | | | |
| 1 | W14 × 132 | W14 × 74 | W12 × 19 | 52.00 |
| 2 | W14 × 132 | W14 × 74 | W12 × 19 | 52.00 |
| 3 | W14 × 82 | W14 × 74 | W12 × 19 | 47.69 |
| 4 | W14 × 82 | W14 × 38 | W12 × 19 | 42.50 |
| 5 | W14 × 38 | W14 × 38 | W12 × 19 | 42.50 |
| 6 | W14 × 38 | W14 × 38 | W12 × 19 | 30.77 |
| 7 | W14 × 38 | W14 × 38 | W12 × 19 | 24.62 |
| 8 | W14 × 26 | W14 × 26 | W12 × 16 | 18.46 |
| 12-Storey BRBF | | | | |
| 1 | W14 × 159 | W14 × 82 | W12 × 19 | 59.00 |
| 2 | W14 × 159 | W14 × 82 | W12 × 19 | 59.00 |
| 3 | W14 × 159 | W14 × 82 | W12 × 19 | 59.00 |
| 4 | W14 × 159 | W14 × 74 | W12 × 19 | 59.00 |
| 5 | W14 × 132 | W14 × 74 | W12 × 19 | 59.00 |
| 6 | W14 × 132 | W14 × 74 | W12 × 19 | 47.69 |
| 7 | W14 × 82 | W14 × 74 | W12 × 19 | 47.69 |
| 8 | W14 × 82 | W14 × 74 | W12 × 19 | 42.50 |
| 9 | W14 × 38 | W14 × 38 | W12 × 19 | 42.50 |
| 10 | W14 × 38 | W14 × 38 | W12 × 19 | 30.77 |
| 11 | W14 × 38 | W14 × 38 | W12 × 19 | 23.00 |
| 12 | W14 × 26 | W14 × 26 | W12 × 16 | 18.46 |
| 15-Storey BRBF | | | | |
| 1 | W14 × 233 | W14 × 82 | W12 × 19 | 67.69 |
| 2 | W14 × 233 | W14 × 82 | W12 × 19 | 67.69 |
| 3 | W14 × 211 | W14 × 82 | W12 × 19 | 67.69 |
| 4 | W14 × 211 | W14 × 74 | W12 × 19 | 67.69 |
| 5 | W14 × 159 | W14 × 74 | W12 × 19 | 67.69 |
| 6 | W14 × 159 | W14 × 74 | W12 × 19 | 59.00 |
| 7 | W14 × 132 | W14 × 74 | W12 × 19 | 59.00 |
| 8 | W14 × 132 | W14 × 74 | W12 × 19 | 59.00 |
| 9 | W14 × 74 | W14 × 38 | W12 × 19 | 59.00 |
| 10 | W14 × 74 | W14 × 38 | W12 × 19 | 46.15 |
| 11 | W14 × 74 | W14 × 38 | W12 × 19 | 46.15 |
| 12 | W14 × 74 | W14 × 38 | W12 × 19 | 42.50 |

Table A2. Cont.

| Stories | Exterior Column | Interior Column | Beam | Cross Section Area of Brace (cm ²) |
|---------|-----------------|-----------------|----------|--|
| 13 | W14 × 26 | W14 × 38 | W12 × 19 | 42.50 |
| 14 | W14 × 26 | W14 × 38 | W12 × 19 | 24.62 |
| 15 | W14 × 26 | W14 × 26 | W12 × 16 | 18.46 |

References

- Funari, M.F.; Pulatsu, B.; Szabó, S.; Lourenço, P.B. A Solution for the Frictional Resistance in Macro-Block Limit Analysis of Non-Periodic Masonry. *Structures* **2022**, *43*, 847–859.
- Mohammadi, A.; Barros, J.A.O.; Sena-Cruz, J. A New Model for Predicting the Shear Strength of RC Beams Strengthened with Externally Bonded FRP Sheets. *Compos. Struct.* **2023**, *319*, 117081. [[CrossRef](#)]
- Karimzadeh, S. Seismological and Engineering Demand Misfits for Evaluating Simulated Ground Motion Records. *Appl. Sci.* **2019**, *9*, 4497. [[CrossRef](#)]
- Altindal, A.; Karimzadeh, S.; Erberik, M.A.; Askan, A.; Anil, O.; Kockar, M.K.; Sahmaran, M. A Case Study for Probabilistic Seismic Risk Assessment of Earthquake-Prone Old Urban Centers. *Int. J. Disaster Risk Reduct.* **2021**, *61*, 102376. [[CrossRef](#)]
- Hoveidae, N.; Fathi, A.; Karimzadeh, S. Seismic Damage Assessment of a Historic Masonry Building under Simulated Scenario Earthquakes: A Case Study for Arge-Tabriz. *Soil Dyn. Earthq. Eng.* **2021**, *147*, 106732.
- Işık, E.; Hadzima-Nyarko, M.; Bilgin, H.; Ademović, N.; Büyüksaraç, A.; Harirchian, E.; Bulajić, B.; Özmen, H.B.; Aghakouchaki Hosseini, S.E. A Comparative Study of the Effects of Earthquakes in Different Countries on Target Displacement in Mid-Rise Regular Rc Structures. *Appl. Sci.* **2022**, *12*, 12495.
- Genç, A.F.; Atmaca, E.E.; Günaydin, M.; Altunişik, A.C.; Sevim, B. Evaluation of Soil Structure Interaction Effects on Structural Performance of Historical Masonry Buildings Considering Earthquake Input Models. *Structures* **2023**, *54*, 869–889.
- Yaghmaei-Sabegh, S.; Daneshgari, S. Residual Displacement Ratios of Highly Damped SDOF Systems by Considering Soft Soil Conditions. *Soil Dyn. Earthq. Eng.* **2023**, *165*, 107741. [[CrossRef](#)]
- Mishra, M. Machine Learning Techniques for Structural Health Monitoring of Heritage Buildings: A State-of-the-Art Review and Case Studies. *J. Cult. Herit.* **2021**, *47*, 227–245.
- Yüksel, N.; Börklü, H.R.; Sezer, H.K.; Canyurt, O.E. Review of Artificial Intelligence Applications in Engineering Design Perspective. *Eng. Appl. Artif. Intell.* **2023**, *118*, 105697.
- Kazemi, F.; Asgarkhani, N.; Jankowski, R. Machine Learning-Based Seismic Response and Performance Assessment of Reinforced Concrete Buildings. *Arch. Civ. Mech. Eng.* **2023**, *23*, 94. [[CrossRef](#)]
- Tapeh, A.T.G.; Naser, M.Z. Artificial Intelligence, Machine Learning, and Deep Learning in Structural Engineering: A Scientometrics Review of Trends and Best Practices. *Arch. Comput. Methods Eng.* **2023**, *30*, 115–159.
- Li, H.; Yang, D.; Hu, T. Data-Driven Model for Predicting the Compressive Strengths of GFRP-Confined Reinforced Concrete Columns. *Buildings* **2023**, *13*, 1309. [[CrossRef](#)]
- Kaya, Ö.; Çodur, M.Y.; Mustafaraj, E. Automatic Detection of Pedestrian Crosswalk with Faster R-CNN and YOLOv7. *Buildings* **2023**, *13*, 1070.
- Yasar, C.; Karuk, V.; Kaplan, O.; Cavdar, E.; Ozdemir, G. Amplification in Mechanical Properties of a Lead Rubber Bearing for Various Exposure Times to Low Temperature. *Buildings* **2023**, *13*, 478. [[CrossRef](#)]
- Afshari, S.S.; Zhao, C.; Zhuang, X.; Liang, X. Deep Learning-Based Methods in Structural Reliability Analysis: A Review. *Meas. Sci. Technol.* **2023**, *34*, 7.
- Koc, A.B.; Erberik, M.A.; Askan, A.; Karimzadeh, S. The Sensitivity of Global Structural Parameters for Unreinforced Masonry Buildings Subjected to Simulated Ground Motions. *Buildings* **2023**, *13*, 2060. [[CrossRef](#)]
- Karimi, N.; Valibeig, N.; Rabiee, H.R. Deterioration Detection in Historical Buildings with Different Materials Based on Novel Deep Learning Methods with Focusing on Isfahan Historical Bridges. *Int. J. Archit. Herit.* **2023**, 1–13. [[CrossRef](#)]
- Bagherzadeh, F.; Shafighfard, T.; Khan, R.M.A.; Szczuko, P.; Mieloszyk, M. Prediction of Maximum Tensile Stress in Plain-Weave Composite Laminates with Interacting Holes via Stacked Machine Learning Algorithms: A Comparative Study. *Mech. Syst. Signal Process.* **2023**, *195*, 110315.
- Mohammadi, A.; Karimzadeh, S.; Amir, S.; Ozsarac, V.; Lourenço, P.B. The Potential of Region-Specific Machine-Learning-Based Ground Motion Models: Application to Turkey. *Soil Dyn. Earthq. Eng.* **2023**, *172*, 108008. [[CrossRef](#)]
- Mojtabaei, S.M.; Becque, J.; Hajirasouliha, I.; Khandan, R. Predicting the Buckling Behaviour of Thin-Walled Structural Elements Using Machine Learning Methods. *Thin-Walled Struct.* **2023**, *184*, 110518. [[CrossRef](#)]
- Noureldin, M.; Ali, T.; Kim, J. Machine Learning-Based Seismic Assessment of Framed Structures with Soil-Structure Interaction. *Front. Struct. Civ. Eng.* **2023**, *17*, 205–223.
- Cardellicchio, A.; Ruggieri, S.; Nettis, A.; Renò, V.; Uva, G. Physical Interpretation of Machine Learning-Based Recognition of Defects for the Risk Management of Existing Bridge Heritage. *Eng. Fail. Anal.* **2023**, *149*, 107237.
- Kilic, G. Assessment of Historic Buildings after an Earthquake Using Various Advanced Techniques. *Structures* **2023**, *50*, 538–560.

25. Naghavi, M.; Rahnavard, R.; Thomas, R.J.; Malekinejad, M. Numerical Evaluation of the Hysteretic Behavior of Concentrically Braced Frames and Buckling Restrained Brace Frame Systems. *J. Build. Eng.* **2019**, *22*, 415–428. [[CrossRef](#)]
26. Yoshino, T.; Karino, Y. Experimental Study on Shear Wall with Braces: Part 2. In *Summaries of Technical Papers of Annual Meeting; Structural Engineering Section, Architectural Institute of Japan*: Tokyo, Japan, 1971; Volume 11, pp. 403–404.
27. Kimura, K.; Yoshioka, K.; Takeda, T.; Fukuya, Z.; Takemoto, K. Tests on Braces Encased by Mortar In-Filled Steel Tubes. In *Summaries of Technical Papers of Annual Meeting; Architectural Institute of Japan*: Tokyo, Japan, 1976; Volume 1041, pp. 1–42.
28. Wei, X.; Bruneau, M. Case Study on Applications of Structural Fuses in Bridge Bents. *J. Bridge Eng.* **2016**, *21*, 05016004. [[CrossRef](#)]
29. Wang, Y.; Ibarra, L.; Pantelides, C. Seismic Retrofit of a Three-Span RC Bridge with Buckling-Restrained Braces. *J. Bridge Eng.* **2016**, *21*, 4016073. [[CrossRef](#)]
30. Wei, X.; Bruneau, M. Analytical Investigation of Buckling Restrained Braces' Applications in Bidirectional Ductile End Diaphragms for Seismic Performance of Slab-on-Girder Bridge. *Eng. Struct.* **2017**, *141*, 634–650. [[CrossRef](#)]
31. Bazaiez, R.; Dusicka, P. Performance Assessment of Multi-Column RC Bridge Bents Seismically Retrofitted with Buckling-Restrained Braces. *Bull. Earthq. Eng.* **2018**, *16*, 2135–2160.
32. Wang, Y.; Ibarra, L.; Pantelides, C. Effect of Incidence Angle on the Seismic Performance of Skewed Bridges Retrofitted with Buckling-Restrained Braces. *Eng. Struct.* **2020**, *211*, 110411.
33. Zhou, Y.; Shao, H.; Cao, Y.; Lui, E.M. Application of Buckling-Restrained Braces to Earthquake-Resistant Design of Buildings: A Review. *Eng. Struct.* **2021**, *246*, 112991.
34. Cao, X.-Y.; Feng, D.-C.; Wang, Z.; Wu, G. Parametric Investigation of the Assembled Bolt-Connected Buckling-Restrained Brace and Performance Evaluation of Its Application into Structural Retrofit. *J. Build. Eng.* **2022**, *48*, 103988.
35. McKenna, F.; Scott, M.H.; Fenves, G.L. Nonlinear Finite-Element Analysis Software Architecture Using Object Composition. *J. Comput. Civ. Eng.* **2010**, *24*, 95–107. [[CrossRef](#)]
36. Baker, J.W. Quantitative Classification of Near-Fault Ground Motions Using Wavelet Analysis. *Bull. Seismol. Soc. Am.* **2007**, *97*, 1486–1501. [[CrossRef](#)]
37. Vafaei, D.; Eskandari, R. Seismic Response of Mega Buckling-restrained Braces Subjected to Fling-step and Forward-directivity Near-fault Ground Motions. *Struct. Des. Tall Spec. Build.* **2015**, *24*, 672–686. [[CrossRef](#)]
38. Manual, A.S. Seismic Provisions for Structural Steel Buildings. *ANSI/AISC* **2005**, 305–341.
39. López, W.A.; Sabelli, R. Seismic Design of Buckling-Restrained Braced Frames. *Steel Tips* **2004**, 78.
40. Uniform Building Code (UBC). *International Conference of Building Officials*; ICBO: Tokyo, Japan, 1997.
41. Coy, B.B.; Richards, P.W. *Buckling-Restrained Braced Frame Connection Design and Testing*; Brigham Young University: Provo, UT, USA, 2007; ISBN 9798662574854.
42. Black, C.; Aiken, I.D.; Makris, N. *Component Testing, Stability Analysis, and Characterization of Buckling-Restrained Unbonded Braces (TM)*; Pacific Earthquake Engineering Research Center: Berkeley, CA, USA, 2002.
43. SAC Joint Venture Protocol for Fabrication, Inspection, Testing, and Documentation of Beam-Column Connection Tests and Other Experimental Specimens; Rep. No. SAC/BD-97; SAC: Richmond, CA, USA, 1997; Volume 2.
44. Yaghmaei-Sabegh, S.; Ranjbari, M.; Neekmanesh, S. Effect of Pulse on Fragility Curves of Buckling-Restrained Braced Frames. *Soil Dyn. Earthq. Eng.* **2023**, *175*, 108262. [[CrossRef](#)]
45. Adamowski, J.; Karapataki, C. Comparison of Multivariate Regression and Artificial Neural Networks for Peak Urban Water-Demand Forecasting: Evaluation of Different ANN Learning Algorithms. *J. Hydrol. Eng.* **2010**, *15*, 729–743. [[CrossRef](#)]
46. Pedregosa, F.; Varoquaux, G.; Gramfort, A.; Michel, V.; Thirion, B.; Grisel, O.; Blondel, M.; Prettenhofer, P.; Weiss, R.; Dubourg, V. Scikit-Learn: Machine Learning in Python. *J. Mach. Learn. Res.* **2011**, *12*, 2825–2830.
47. Ke, G.; Meng, Q.; Finley, T.; Wang, T.; Chen, W.; Ma, W.; Ye, Q.; Liu, T.-Y. LightGBM: A Highly Efficient Gradient Boosting Decision Tree. In *Advances in Neural Information Processing Systems*; Guyon, I., Luxburg, U.V., Bengio, S., Wallach, H., Fergus, R., Vishwanathan, S., Garnett, R., Eds.; Curran Associates: New York, NY, USA, 2017; pp. 3146–3154.
48. Lundberg, S.M.; Su-In, L. A Unified Approach to Interpreting Model Predictions. In *Proceedings of the 31st Conference on Neural Information Processing Systems (NIPS 2017)*, Long Beach, CA, USA, 4–9 December 2017.
49. Veismoradi, S.; Darvishan, E. Probabilistic Seismic Assessment of Mega Buckling-Restrained Braced Frames under near-Fault Ground Motions. *Earthq. Struct.* **2018**, *15*, 487–498.

Disclaimer/Publisher's Note: The statements, opinions and data contained in all publications are solely those of the individual author(s) and contributor(s) and not of MDPI and/or the editor(s). MDPI and/or the editor(s) disclaim responsibility for any injury to people or property resulting from any ideas, methods, instructions or products referred to in the content.